Measurement Science and Technology

100 year anniversary
Measurement Science and Technology

PAPER • OPEN ACCESS

Lagrangian particle tracking in the atmospheric surface layer

To cite this article: Nicholas Conlin *et al* 2024 *Meas. Sci. Technol.* **35** 095803

OPEN ACCESS
IOP Publishing
Measurement Science and Technology
Meas. Sci. Technol. **35** (2024) 095803 (15pp)
https://doi.org/10.1088/1361-6501/ad56ac

Lagrangian particle tracking in the atmospheric surface layer

Nicholas Conlin[1], Hannah Even[1], Nathaniel J Wei[2], N Agastya Balantrapu[3] and Marcus Hultmark[1,*]

[1] Department of Mechanical and Aerospace Engineering, Princeton University, Princeton, NJ, United States of America
[2] Andlinger Center for Energy and the Environment, Princeton University, Princeton, NJ, United States of America
[3] Department of Mechanical Engineering, University of Utah, Salt Lake City, UT, United States of America

E-mail: hultmark@princeton.edu

Received 21 February 2024, revised 17 May 2024
Accepted for publication 11 June 2024
Published 26 June 2024

Abstract

Field measurements in the atmospheric surface layer (ASL) are key to understanding turbulent exchanges in the atmosphere, such as fluxes of mass, water vapor, and momentum. However, current field measurement techniques are limited to single-point time series or large-scale flow field scans. Extending image-based laboratory measurement techniques to field-relevant scales is a promising route to more detailed atmospheric flow measurements, but this requires significant increases in the attainable measurement volume while keeping the spatiotemporal resolution high. Here, we present an adaptable particle tracking system using helium-filled soap bubbles, mirrorless cameras, and high-power LEDs enabling volumetric ASL field measurements. We conduct analyses pertinent to image-based field measurement systems and develop general guidelines for their design. We validate the particle tracking system in a field experiment. Single-point Eulerian velocity statistics are presented and compared to data from concurrently operated sonic anemometers. Lagrangian displacement statistics are also presented with a comparison to Taylor's theory of dispersion. The system improves the state-of-the-art in field measurements in the lower atmosphere and enables unprecedented insights into flow in the ASL.

Keywords: turbulence, atmospheric surface layer, particle tracking

1. Introduction

Turbulent motions drive transport in the atmospheric surface layer (ASL). Understanding this process is essential for applications such as numerical weather prediction [1], wind energy optimization [2, 3], and insect olfactory search [4]. Laboratory experiments and numerical simulations of the ASL face significant limitations because of the restricted range of scales that can be achieved and the inability to replicate complex boundary conditions. This makes field experiments invaluable [5].

Prevailing field measurement techniques are confined to single-point time series employing sonic, cup, or hot-wire anemometers, with a range of temporal resolutions. These techniques are fundamental to current understanding of the ASL but provide limited spatial resolution and information. Large-scale flow field scans using lidar or sodar depend on the reflectance properties of the medium and have a low signal-to-noise ratio, obfuscating small-scale structure [5]. More broadly, the vast majority of existing measurements are

[*] Author to whom any correspondence should be addressed.

Eulerian, despite the relevance of Lagrangian statistics for passive scalars [6] and turbulence modeling [7]. Canopy layers are one exemplary system where Lagrangian field measurements have lagged laboratory experiments [8]. Drawing on advances in laboratory experimental techniques and previous field experiments, we present a system for ASL measurements based on three-dimensional (3D) tracking of helium-filled soap bubbles, capable of providing Eulerian and Lagrangian statistics over a broad range of scales.

Measurement techniques based on imaging tracer particles offer high spatiotemporal resolution and are standard for laboratory experiments (see [9, 10] for recent reviews). However, they have been limited to small volumes ($\sim 1\,\mathrm{m}^3$) and are impractical to scale up to field relevance. Field experiments using image-based techniques have only recently become viable, primarily enabled by flexible camera calibration techniques [11] and unconventional tracer particles [12]. Natural snowfall has been used as seeding particles to perform two-dimensional particle image velocimetry (PIV) on a full-scale horizontal axis wind turbine [12] and the ASL [13]. PIV is based on correlating the motion of particles within an interrogation window. A dense uniform seeding is required, which is nearly impossible to artificially generate in the field.

Lagrangian particle tracking (LPT) is an alternative approach that follows individual tracer particles. LPT is suited to field experiments because it is naturally extended to 3D, and the seeding density can be sparse and non-uniform [10]. We note that particle tracking velocimetry (PTV) is a commonly used acronym for the same technique. We use the more general descriptor LPT because we do not only report velocity statistics. Recently, 3D LPT field experiments with natural snowfall have been conducted to study snow-settling dynamics [14]. Artificial snow has also been used to study the wake of a vertical axis wind turbine [15]. Using natural snowfall is ingenious but experiments are contingent on favorable weather conditions. Artificial snow may be deployed arbitrarily but the machines are bulky, and the particles exhibit a broad distribution of properties, posing challenges in characterizing tracing fidelity. Previous measurements with artificial snow have been confined to the mean flow [15]. In general, the high settling velocity of snow particles ($\sim 0.6\,\mathrm{ms}^{-1}$ [12]) limits applications to velocimetry. Particles deviate from the flow in the vertical direction, complicating interpretations of vertical fluxes. Large (25 mm) air-filled soap bubbles have also been used to study the ASL using LPT in a 4 m $\times$ 2 m $\times$ 2 m domain [16]. We build on this approach by simultaneously increasing the measurement volume, decreasing the particle size, and using neutrally buoyant particles.

The remainder of the paper is organized as follows. In section 2 the LPT system design is discussed, including hardware and software. This includes camera sizing section 2.2, tracer particle selection section 2.3, illumination section 2.4, camera calibration section 2.5, and particle triangulation (section 2.6. Evaluation of the system in a field experiment is given in section 3. Concluding remarks are given in section 4.

2. System design

2.1. System overview

The primary hardware components of the LPT system are shown in figure 1. The flow is seeded with helium-filled soap bubbles of diameter 8.0 ± 0.25 mm and illuminated by nine 500 W LED lamps with a beam angle of 120° (TYCOLIT B0B3DPTXVX). The lights are powered by a 9 kW gas generator (Predator 59 206). Four mirrorless cameras (Canon EOS R5) are placed around the 8 m $\times$ 8 m $\times$ 4 m measurement volume and image the light scattered by the bubbles. Images are captured at a resolution of 4096 $\times$ 2094 pixels and a frame rate of 120 Hz. Cameras are equipped with a variable focal length lens (Canon RF 24-105 mm F4 L IS USM), typically operated at 30 mm. This yields a resolution of approximately 0.7 mm per pixel in the center of the measurement domain based on the pixel pitch of 4.4 µm and a typical working distance of 10 m . The aperture is set to $f_{\#} = 8$. Each camera is operated on battery power and records data to an onboard 325 GB memory card (ProGrade CFexpress). At the specified recording settings this allows up to 30 min of total recording.

Subsequent sections delve into the system's design. Each section includes a brief analysis of the general design aspects of image-based field measurement systems, accompanied by a succinct set of guidelines when feasible. We emphasize that field experiments invariably require flexibility due to inherently variable conditions, often rendering the optimal design infeasible or impractical. Therefore, having a guiding set of principles and an understanding of system sensitivity to adjustments is useful.

2.2. Camera sizing

Optical field experiments require cameras that can simultaneously image a large volume and resolve small scales. Imaging a large range of scales requires a camera sensor with many pixels. However, the flow must also be temporally resolved. Data transfer rates limit the maximum frame rate of high-resolution cameras. In high Reynolds number laboratory experiments temporal resolution requirements are very strict (e.g. 70 kHz [17]) because a large range of scales is forced into a small volume. In the ASL the fastest timescales are more modest. The Kolmogorov time scale is O(0.1 s) using air at standard conditions and estimating the Kolmogorov length scale to be O(1 mm) [5]. Frame rates on the order of 100 Hz may be acceptable. Commercial mirrorless cameras are capable of recording 4 K resolution images at 120 Hz and greatly reduce the complexity and cost of the experimental setup. Images are recorded to onboard storage, cameras run on battery power, and the cameras are designed to operate in field conditions.

2.3. Tracer particle selection and production

Conventional tracers for gas flows, like polystyrene spheres and liquid droplets, are $\sim$1 µm in diameter [18]. These small

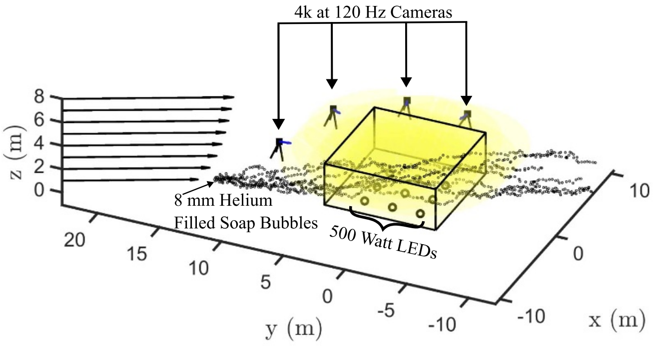

Figure 1. Schematic of the LPT system with primary hardware components.

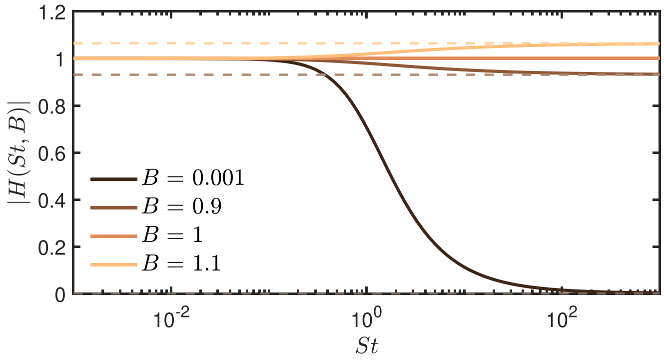

Figure 2. Transfer function description of tracing fidelity for different density ratios. Dashed lines are asymptotic limits from equation (5). As $St \to \infty$ heavy particles attenuate velocity fluctuations, and light particles amplify them.

particles have high tracing fidelity but scatter insufficient light for large volumes. A fundamental challenge in increasing measurement volumes to ASL-relevant scales is the trade-off between tracing fidelity and illumination. Larger particles scatter more light but follow the flow less faithfully. In this section, we analyze the relevant dynamics of inertial particles and offer guidelines on particle selection.

2.3.1. Inertial particle dynamics. We begin by summarizing previous results on inertial particle dynamics [19, 20] using the Maxey–Riley equation [21], which predicts the motion of a small spherical particle of density ρ_p, diameter d_p, and velocity V_p in a fluid of dynamic viscosity μ, density ρ_f and velocity U. After introducing corrections for finite particle Reynolds number, the force balance reads [19]

$$m_p \frac{\mathrm{d}V_p}{\mathrm{d}t} = 3\pi\mu d_p \phi(\mathrm{Re}_p)(U - V_p) + \frac{m_f}{2}\left(\frac{\mathrm{D}U}{\mathrm{D}t} - \frac{\mathrm{d}V_p}{\mathrm{d}t}\right) + m_f \frac{\mathrm{D}U}{\mathrm{D}t} + 3\pi\mu d_p \int_0^t K(t-\tau)\frac{\mathrm{d}(U - V_p)}{\mathrm{d}\tau}\mathrm{d}\tau \tag{1}$$

where $m_p = \pi\rho_p d_p^3/6$ is the particle mass and $m_f = \pi\rho_f d_p^3/6$ is the mass of an equivalent sized fluid element. The first term on the right-hand side represents viscous (Stokes) drag on the particle with a correction ϕ based on the particle Reynolds number Re_p. The second term is the added mass force for a sphere [22]. The third term is due to local fluid stresses, i.e. the force felt by a fluid element in an undisturbed flow. The last term is the history force with a decaying memory kernel $K(t-\tau)$. For a characteristic flow frequency ω dimensional analysis suggests two critical parameters to predict the ratio V_p/U, which quantifies the particle tracing fidelity: the Stokes number St and the density ratio B

$$St = \frac{m_p\omega}{3\pi\mu d_p} \qquad B = \frac{\rho_f}{\rho_p}. \tag{2}$$

Transfer function analysis shows how the influence of different forces varies with St [19, 20, 23, 24]. Inserting $V_p = \hat{V}_p\mathrm{e}^{-\mathrm{i}\omega t}$ and $U = \hat{U}\mathrm{e}^{-\mathrm{i}\omega t}$ into equation (1) the ratio $H = \hat{V}_p/\hat{U}$ can be derived, which describes the attenuation, or amplification, of fluid velocity fluctuations by the particle

$$H(St, B) = \frac{\frac{2}{3} + (1-i)\sqrt{StB} - iStB}{\frac{2}{3} + (1-i)\sqrt{StB} - iSt\left(\frac{2}{3} + \frac{1}{3}B\right)} \tag{3}$$

where $i = \sqrt{-1}$. The asymptotic behavior of the history force has been used, resulting in terms $\propto (1-i)\sqrt{StB}$ [19]. Finite Re_p corrections are neglected in the Stokes drag force for simplicity since they do not change the asymptotic arguments given.

At small St, $|H(St \to 0, B)| \to 1$, implying perfect tracing fidelity for very slow fluctuations. As St increases the particle exhibits qualitatively different behavior depending on the density ratio. For conventional gas flow tracers with $StB \ll 1$ the transfer function simplifies to

$$H_c(St) = \frac{1}{1 - iSt} \tag{4}$$

which describes a low-pass filter behavior where the particle response decays at high excitation frequency, $|H_c(St \to \infty)| \to 0$. Stokes drag dominates the force balance, inducing an acceleration that counters any differences in the particle and fluid velocity. The particle dynamics are governed by a relaxation time scale, responding to fluctuations slower than the relaxation time and not responding to faster fluctuations. For example, a liquid droplet in air has $B \approx 10^{-3}$. The behavior of such a particle is shown in figure 2, where the condition $St \sim 1$ marks the decay of particle response.

The asymptotic behavior is fundamentally altered when $B \approx 1$. At large St, the response approaches a finite limit governed only by the density ratio

$$H(St \to \infty, B) \to \frac{3B}{2+B}. \tag{5}$$

The finite limit represents the influence of added mass and fluid stress. Analogous to how the drag force induces an acceleration to reduce the slip velocity, added mass responds to slip accelerations. The effect is potent at high St. Particles with $0.93 \leqslant B \leqslant 1.07$ have $0.95 \leqslant |H(St \to \infty, B)| \leqslant 1.05$. The approach to a limiting value is shown in figure 2 for

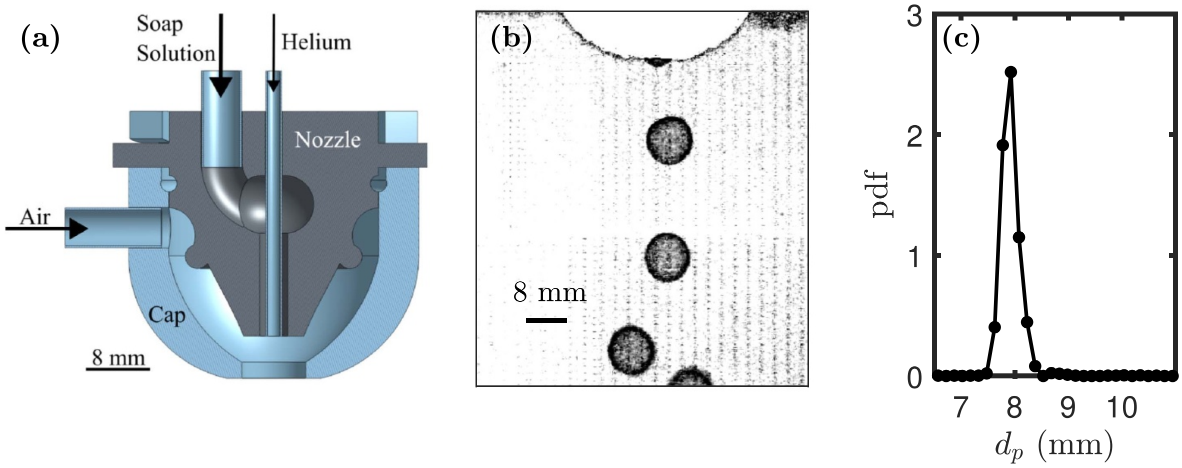

Figure 3. (a) Bubble generator design. (b) Example shadowgraph image of bubbles. (c) Distribution of bubble diameters.

several values of $B \approx 1$. Since $|H(St,B)|$ always increasingly departs from 1 with increasing St the limit in equation (5) is a conservative bound on the tracing fidelity. However, there are some caveats.

2.3.2. Finite size effects. The limit in equation (5) would suggest that particle response is independent of d_p at high St, conflicting with the intuitive idea that particles cannot respond to fluctuations with characteristic scales smaller than their diameter. The d_p independence is a result of using equation (1), which assumes a particle much smaller than any flow length scale. For this assumption to hold $d_p/\eta < 1$ is required, where η is the Kolmogorov length scale. When $d_p/\eta > 1$ previous studies have shown that neutrally buoyant particles experience an acceleration that is averaged over scales smaller than the diameter. Across experiments and simulations, the ratio of particle to fluid acceleration variance against d_p/η collapses on a single curve for $d_p/\eta < 10$ well predicted by an averaging model [17, 25–28]. Arguments supporting a universal averaging model stem from Kolmogorov's similarity hypotheses [25]. Transfer function analysis is complimentary, providing physical insight into the responsible forces. In conclusion, similar to conventional tracers described by a low pass filter in time with a cut-off time scale based on the Stokes number, finite-sized neutrally buoyant particles act as a low pass filter in space with a cut-off scale d_p.

The importance of averaging over the smallest scales depends on the quantity one wants to measure. For viscous scale phenomena, like fluid particle accelerations, small-scale averaging has a noticeable impact [17]. However, in the ASL focus frequently lies on low-order statistics of single-point velocity fluctuations, which are governed by the largest turbulent scales [29]. Indeed, sonic anemometers are the standard for ASL measurements and average over a path length of ∼10 cm [30]. In our experiments, to balance finite-size effects with illumination requirements we target $d_p/\eta \leqslant 10$ while maintaining $0.93 \leqslant B \leqslant 1.07$.

2.3.3. Tracer production. To meet these requirements we use helium-filled soap bubbles (HFSBs). HFSBs have been used extensively in wind tunnels [31–33] and have several attractive qualities for field experiments. Particle properties can be tuned, the environmental impact is limited to trace amounts of soap solution, and the production hardware is reasonably portable. Knowing that η is O(1 mm) in the ASL, an HFSB generator was designed to produce diameters between 5 and 10 mm. A section view of the generator design is shown in figure 3(a). The design draws from [34], with two primary components: a nozzle that produces concentric flows of helium and soap solution, and an interchangeable cap that directs air to the exit orifice. The physical mechanism underlying HFSB production has recently been explained via the Rayleigh-Plateau instability [35]. HFSB generator components were manufactured using a 3D resin printer (Form Labs V2). Printable files of the generator parts are available in the Supplemental Material.

We inject helium via a 14-gauge syringe that runs through the entire nozzle. Stainless steel inserts are used for attaching tubing to the gas ports. By using different caps and controlling the flow rates of helium, bubble solution, and air the HFSB properties can be manipulated. Gas flow rates into the nozzle are controlled by flow controllers for air (Omega FMA5527A) and helium (Omega FMA5520A). Helium is drawn from a 552 L gas cylinder (Grainger 29YF75) and air is supplied by a 30.3 L compressor (Husky 1002-714-648). Gas pressures are reduced via a regulator and passed through 40 µm particulate filters. The bubble solution contains concentrated soap (JOYIN J-BCS1) and water with a 10% by volume ratio. The bubble solution flow rate is controlled with a syringe pump (Just Infusion NE-300).

The bubble diameter was designed around the criterion $d_p/\eta \leqslant 10$ and ease of particle identification in camera images. The latter requirement is discussed in the next section. A target bubble diameter of 8 mm was selected. The bubble diameter distribution was measured by shadowgraphy (figure 3(b)) and is shown in figure 3(c). The mean diameter is $\langle d_p \rangle =$

8.0 mm and the standard deviation is $\sigma_{d_p} = 0.25$ mm. The ratio $\sigma_{d_p}/\langle d_p \rangle \approx 3\%$ is comparable to previous HFSB generator designs [34, 36], indicating reasonable uniformity of bubble size. The production rate of the generator measured by high-speed video is $\dot{N} = 88$ bubbles per second. Near neutral buoyancy is achieved by the appropriate specification of helium ($\dot{m}_{\mathrm{He}}$) and soap solution ($\dot{m}_{\mathrm{S}}$) mass flow rates [36]. Equating input mass flow to the bubble outflow,

$$\dot{m}_{\mathrm{He}} + \dot{m}_{\mathrm{S}} = \frac{\pi}{6}\rho_p d_p^3 \dot{N}. \tag{6}$$

Mass flow rates were specified as $\dot{m}_{\mathrm{He}} = 0.028\,\mathrm{g\,s^{-1}}$ and $\dot{m}_{\mathrm{S}} = 0.0032\,\mathrm{g\,s^{-1}}$, which yields $B \approx 0.94$ at relevant field conditions.

2.3.4. Bubble breakup. We note that soap bubbles could potentially be broken up by turbulent fluctuations, invalidating the rigid sphere assumption used in the analysis of particle dynamics. The Weber number quantifies the relative strength of deforming turbulent fluctuations to restoring surface tension forces. For a particle with a diameter greater than the Kolmogorov scale the Weber number can be written as [37]

$$We = \frac{\rho_f (\varepsilon d_p)^{2/3} d_p}{\gamma} \tag{7}$$

where ε is the dissipation rate of turbulent kinetic energy and γ is the surface tension. Estimating the Kolmogorov length scale as O(1 mm), using air at standard conditions, and a surface tension of 30 mN m^{-1} [38] the Weber number is O(10^{-4}). This is well within the regime where a rigid sphere assumption is valid [37].

2.4. Illumination and particle identification

To ensure that particles can be reliably identified in camera images, they should be bright and several pixels in diameter when imaged. A particle at location $\mathbf{x_p}$ being illuminated by a continuous, non-collimated spherical light source of power P at a location $\mathbf{x_L}$ produces a mean exposure $\bar{\epsilon}$ on a camera sensor at location $\mathbf{x_c}$ that can be approximated by [18]

$$\bar{\epsilon} \sim \left(\frac{P\delta t_e}{||\mathbf{x_p} - \mathbf{x_L}||^2}\right)\left(\frac{d_p^2}{d_I^2 + d_\tau^2}\right)\left(\frac{f^2}{||\mathbf{x_p} - \mathbf{x_c}||^2 f_\#^2}\right) \tag{8}$$

where δt_e is the camera exposure time, f is the camera focal length, d_I is the geometric particle image diameter, and d_τ is the diffraction spot size. The scattering regime is assumed to be geometric [18]. We analyze this equation intending to optimize illumination, particle characteristics, and camera settings under the constraints of field experiments. A complimentary analysis for laboratory experiments has recently been given [35].

A significant challenge to optical field experiments is limited access to electrical power for illumination, an issue exacerbated by large measurement volumes. The first parentheses in equation (8) represent the intensity of light at the particle location. To minimize the required light power, particles must be close to the illumination source. This suggests placing a light source directly adjacent to the measurement domain. Such a placement necessitates a very large beam angle. Even if such a wide angle were feasible much of the light would illuminate regions outside the measurement domain. A more directed approach is to use multiple light sources with a narrower beam angle. Using continuous light sources is simpler than synchronizing the camera array to pulsed light sources. While pulsed sources would significantly reduce the total illumination energy, the peak power would not change, which is the primary limiting factor in field experiments.

The second set of parentheses in the mean exposure equation describes the influence of the physical particle diameter and the particle image size. In the numerator, d_p^2 accounts for an increase in scattered light with particle size. The denominator is the total imaged particle diameter on the camera sensor (squared), with contributions from geometric d_I and the diffraction effects d_τ. Increasing the particle image diameter spreads light over a larger area, resulting in a lower mean exposure. For conventional tracers imaged with magnification M we have $d_I = Md_p$ so that the mean exposure becomes independent of the particle diameter for very large particles ($Md_p \gg d_\tau$) [39]. Eventually, increases in scattered light are counteracted by the enlarged image diameter. Soap bubbles exhibit slightly more complex light-scattering properties but a similar principle holds. Light entering and exiting the soap film is partially reflected, leading to pairs of high-intensity lobes, often referred to as 'glare points.' At a viewing angle of 90 deg the distance between glare points on the camera sensor is $d_g = M\sqrt{2}d_p/2$ [40]. Two imaging regimes are present. When $d_g \ll d_\tau$ the particle image is diffraction dominated and the intensity distribution has a single peak. Conversely, when $d_\tau \ll d_g$ pairs of glare points give rise to an intensity distribution with multiple peaks. Multi-modal intensity distributions make particle identification difficult. On the other hand, the diffraction-dominated regime ($d_g \ll d_\tau$) requires small particles or large $f_\#$, which both decrease the mean exposure. To maximize the mean exposure without producing a multi-modal distribution we target

$$d_\tau = d_g. \tag{9}$$

Matching the diffraction spot size to the glare point spacing, i.e. equation (9), throughout the entire measurement domain is often infeasible. For $M \ll 1$ the diffraction spot size is nearly independent of M so $d_g/d_\tau \propto M$. Particles closer to the camera have more distinct glare points and particles further away are increasingly diffraction-dominated. Weak deviations from equation (9) can be compensated in post-processing, provided the particles remain bright enough to be identified. An inability to identify particles, because they are too dim, would be catastrophic for effective particle tracking, so we err on the side

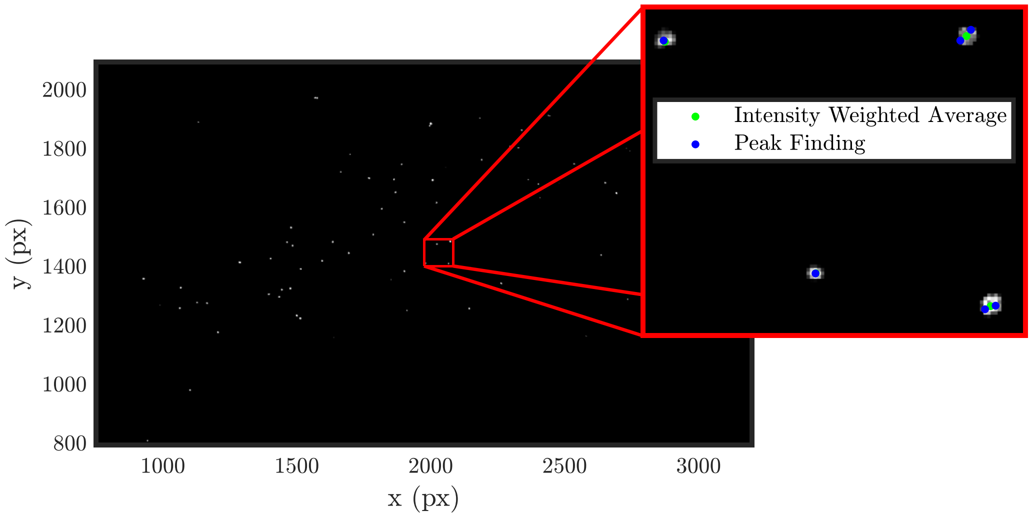

Figure 4. Particle identification procedure to associate one particle with each set of glare points. Left shows an image after pre-processing. The right shows a zoomed-in view detailing the particle-finding procedure. Particles with a single peak use a standard Gaussian peak fit. Particles with multiple peaks are identified with an intensity-weighted average.

of observing glare points, with some extra logic in the particle identification algorithm.

The last set of parentheses in equation (8) is the square of the ratio of the physical aperture area to the distance from the camera to the particle. It suggests using short working distances and a large aperture (small $f_\#$) to maximize the brightness of observed particles. The working distance and focal length are primarily dictated by the scale resolution requirements discussed in section 2.2. The $f_\#$ should be specified taking into account depth of field requirements, diffraction spot size, and brightness of particle images.

In our experiments the final choice of $f_\# = 8$ was determined by imaging particles in field-representative conditions. Depth of field was assessed by moving a 25 mm checkerboard calibration target throughout the measurement domain and checking that edges remained clear. Diffraction spot size and particle brightness were assessed directly from images. Various formulas relating the diffraction spot size and depth of field to $f_\#$ for monochromatic light sources can be found in the literature (e.g. [18]). These are useful for initial estimates but assessment under field-representative imaging conditions is advised. Ultimately, the goal of the illumination and optical setup is to ensure that particles can be reliably identified in camera images.

An example image from field experiments is shown in figure 4 after pre-processing, including background subtraction, masking of light sources, and median filtering. The image is cropped because the camera field of view is larger than the measurement domain to minimize edge distortions. Contrast has been enhanced for illustration. Particles should be much brighter than the background for easy identification. The observed bubble intensity is 35 ± 10 counts while the noise from particulate in the air is 1 ± 1 counts after pre-processing, suggesting that image signal-to-noise ratios are generally large enough to identify particles. Particle centers are first identified with a standard Gaussian peak fitting [41]. The results are shown in a zoomed-in view in figure 4. Some particles show multiple maxima, a sign of glare points, and thus that equation (9) is qualitatively applicable. To identify the particle center the position is computed as an intensity-weighted average when adjacent peaks are closer than one bubble diameter. Sparse seeding makes the distinction between glare point pairs and separate particles unambiguous, as shown in figure 4. Reconstruction of the 3D particle point cloud from image particle centers can then be performed with an appropriate camera calibration.

2.5. Camera calibration and synchronization

Calibrating cameras in field experiments poses challenges as the precise measurement of a calibration target's position is not feasible. Unlike typical laboratory calibration schemes requiring known target positions, field studies employ an unstructured approach, determining camera parameters from images of a calibration object at arbitrary positions. Calibration schemes using a checkerboard target [42] and calibration wand [11] have been developed. In volumetric calibrations, wand techniques offer the advantage of arbitrary target viewing angles, requiring identification only of the wand endpoints. In contrast, checkerboard-style calibrations require all cameras to capture a target plane, which is infeasible for camera arrangements with large angular separation. We perform a wand wave calibration using a 0.653 m long PVC pipe. Calibration videos are recorded where the wand is waved throughout the measurement domain by hand. Camera models are fit from identified wand endpoints using the EASYWAND tool from [11]. A Direct Linear Transform (DLT) model is used, with no distortion corrections.

Camera synchronization is performed with a dual hardware and optical approach. Hardware synchronization is performed using a trigger box (ESPR), which is intended to simultaneously trigger all the cameras. In practice we find cameras are offset by up to 10 frames. Therefore, a refined synchronization is performed in post-processing using a multicolored blinking light in the measurement domain. One camera is set as the primary and the blinking signal from each camera is cross-correlated to find the frame offset that maximizes the cross-correlation. A detailed description of camera synchronization is given in appendix A.

2.6. Triangulation and tracking

For every identified particle in camera images, a 3D ray emanating from the camera can be associated using the DLT equations. By searching for rays that nearly intersect, particle positions in 3D space can be identified. The open-source implementation (4D-PTV) of the ray traversal algorithm from [43] is used to triangulate particles from sets of camera rays. Rays are moved through a discretized digital measurement domain. Voxels with multiple ray traversals are candidates for particle locations. Particle candidate quality is determined by how many rays traverse their voxel of interest and how close the rays are to intersecting. More rays at a voxel indicate that more cameras agree that a particle could be at that location and near intersections indicate close agreement in particle position across cameras. We require a minimum of 3 rays to intersect a voxel for triangulation and the maximum distance between rays is 7 mm. The ray traversal approach was selected because it is objective, computationally efficient, and flexible. Simpler approaches to triangulation using epipolar geometry are tied to the ordering of cameras and identified particles, making them non-objective [43]. More sophisticated triangulation routines based on tomographic principles, such as Shake the Box (STB) [44], are optimized for higher seeding density.

The output of the triangulation routine is a 3D point cloud of particles in each frame. Particles are subsequently tracked to obtain Lagrangian trajectories. Each track is initiated with a nearest-neighbor approach and subsequent frames use a 2-frame kinematic prediction [41]. The prediction assumes negligible acceleration to predict particle positions in the next frame. Tracks are continued by finding the particle in the next frame which is closest to the predicted position, within a maximum distance of 10 cm. Velocities are computed by convolving trajectories with a Gaussian kernel [45]. The convolution filter width is always smaller than the smallest time scale in the flow by a factor of 3 so attenuation of small-scale features by temporal filtering is negligible [46].

3. Field evaluation

3.1. Experimental setup and ambient conditions

A field campaign was conducted in early October 2023 at Island Beach State Park in New Jersey, USA to evaluate the LPT system. The field site is on a narrow strip of land between the Atlantic Ocean and the continental USA. Satellite imagery of the experiment location is shown in figure 5(a). Experiments were conducted at the southern tip of the park. An aerial photo of the experiment site is shown in figure 5(b). The beach site is adjacent to the ocean, approximately 10 m from the waterline. The measurement domain was positioned on the beach about 1.5 m above sea level to avoid rising tides. The terrain close to the site is relatively flat with small undulations in the sand. Larger dunes and vegetation are present 300 m to the east.

The setup of the experiment is shown in figure 6(a). Upon arrival at the beach, a tower was erected with two sonic anemometers (Campbell CSAT3) at $z = 0.89$ m and $z = 1.9$ m sampling at 20 Hz. The measurement domain extent was marked by flags and the illumination LEDs were positioned in a 3×3 grid with a 2 m spacing. The synchronizing LED was attached to a vertical stake in the center of the measurement domain. Cameras were placed along a 90° arc with a 10 m working distance to the center of the measurement domain. The bubble generator was placed on a stand approximately 14 m upstream from the center of the measurement domain. Figure 1 is a schematic of the setup during field experiments. Aligning the bubble trajectories to the center of the domain required occasional repositioning. This can be observed in figure 6(a) where the HFSB plume is not centered on the measurement domain. The HFSB generator was run for several minutes before data collection to avoid inconsistent production during start-up. The entire system was assembled and dismantled during each evening of the field campaign, emphasizing its flexibility to be deployed at arbitrary locations.

Weather conditions during data collection are shown in figures 6(b)–(d) using a five-minute moving average on sonic anemometer time series including the mean wind speed U, the wind direction θ, and the sonic temperature T. A ten-minute window of bubble recordings is selected when ambient conditions are relatively stable, indicated by the blue rectangle in figure 6. Mean wind speeds during this period were $2.14\,\mathrm{m\,s^{-1}}$ at the lower sonic ($z = 0.89$ m) and $2.47\,\mathrm{m\,s^{-1}}$ at the upper sonic ($z = 1.9$ m). Relevant turbulence scales computed by sonic anemometers are shown in table 1 with comparison to the characteristic scales of the LPT system. Generally, the flow is well resolved in time, but the finite size of the particles and positional noise limit the smallest length scales resolved. Closer to the surface η decreases and these effects are increasingly relevant.

3.2. Triangulation and tracking statistics

Particle positions are extracted from the camera images and subsequently triangulated and tracked. Tracks shorter than 17 frames are discarded, based on the minimum convolution fit window of 12 frames and an imposed minimum track length of 5 frames after convolution. The total number of particles that are successfully triangulated and tracked is 7 732 681 with 98% falling within the designated 8 m × 8 m × 4 m measurement domain. The number of trajectories is 83 358. Example HFSB trajectories are shown in figure 7(a) colored by speed. The coordinate system has been rotated so that x is the streamwise direction, y is the spanwise direction, and z is the vertical. There is noise present in the velocity estimates, which can be

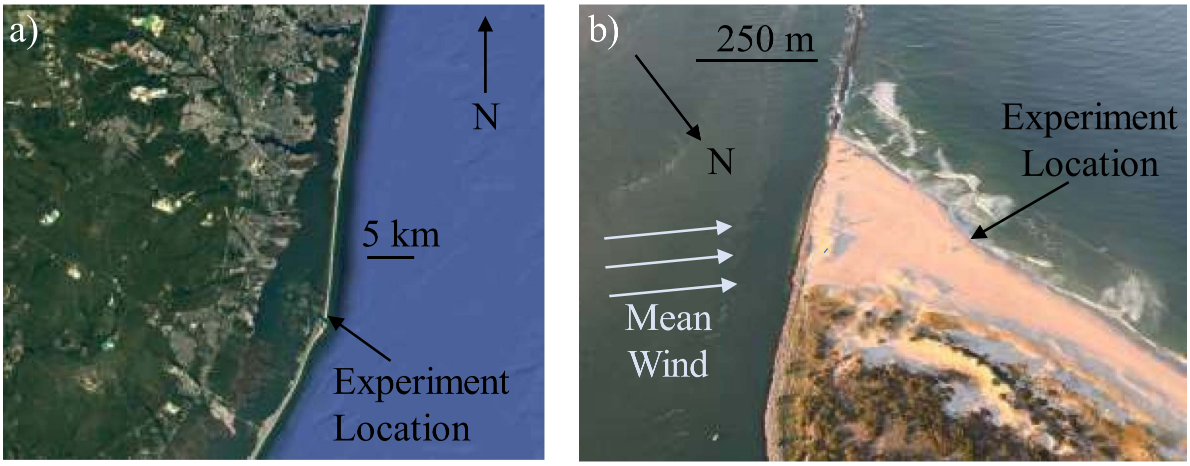

Figure 5. Images of the field campaign location. (a) Satellite imagery of the field campaign location showing surrounding geography. (b) Aerial photo of the experiment location on 9 October 2023 with mean wind direction during bubble data collection indicated.

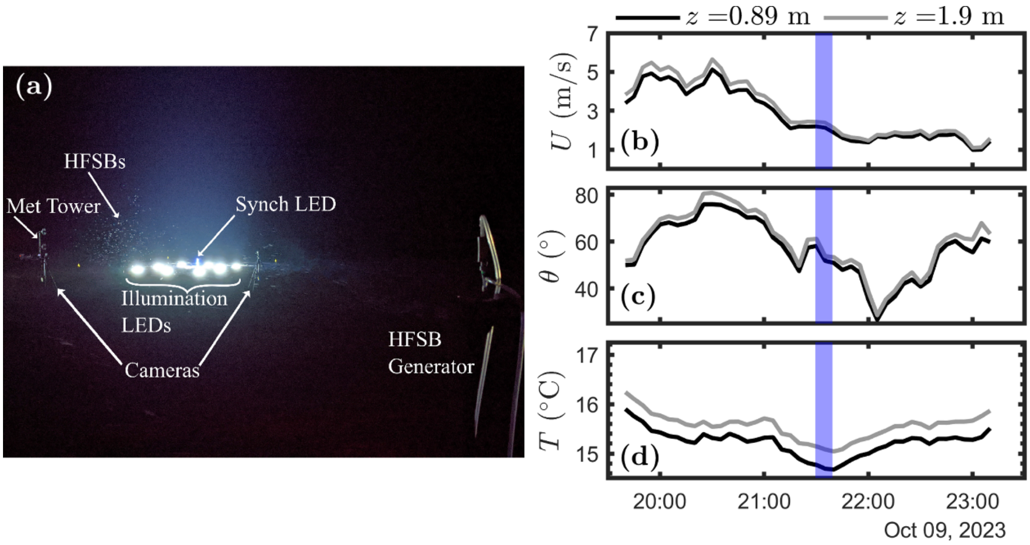

Figure 6. (a) Photograph of field-experiment setup, viewed upwind from the HFSB generator. A schematic of the setup is shown in figures 1(b)–(d) Time series of sonic anemometer data at two different heights above the surface. A five-minute moving average is applied. The blue rectangle indicates the period of bubble data collection. Wind direction θ is measured clockwise from north, as indicated in figure 5(b).

Table 1. table of turbulent and LPT scales. Kolmogorov scales are estimated using the second-order structure function from sonic anemometer time series, converted to spatial increments using Taylor's hypothesis. The friction velocity is estimated by assuming a constant stress layer, e.g. $u_\tau = \sqrt{|\langle uw\rangle|}$. Here Δt_c is the time step between camera frames, $||\mathbf{e_x}||$ is the position uncertainty magnitude and $||\mathbf{e_u}||$ is the velocity uncertainty magnitude. See appendix B for uncertainty estimation.

Height (m)	τ_η (s)	η (mm)	u_τ (m/s)	$\Delta t_c/\tau_\eta$	d_p/η	$\|\|\mathbf{e_x}\|\|/\eta$	$\|\|\mathbf{e_u}\|\|/u_\tau$
0.89	0.050	0.85	0.13	0.17	9.4	4.5	0.80
1.93	0.090	1.1	0.12	0.09	7.0	3.5	0.86

observed from occasional spikes in the speed. We find these are coincident with changes in the observed intensity distribution for a particle. When the intensity distribution shifts from single peak to multi-modal the identified particle position is slightly perturbed. The uncertainty in the velocity estimate due to uncertainties in particle positions is detailed in appendix B based on a statistical analysis.

The track length histogram is shown in figure 7(b). Generally, the number of tracks decreases with increasing track length as any failure in the particle identification, triangulation, or tracking procedure results in a truncated trajectory. The rate at which the histogram decays is an indicator of the probability of connecting tracks in a subsequent frame. Approximately exponential behavior from 100 to 400 frames

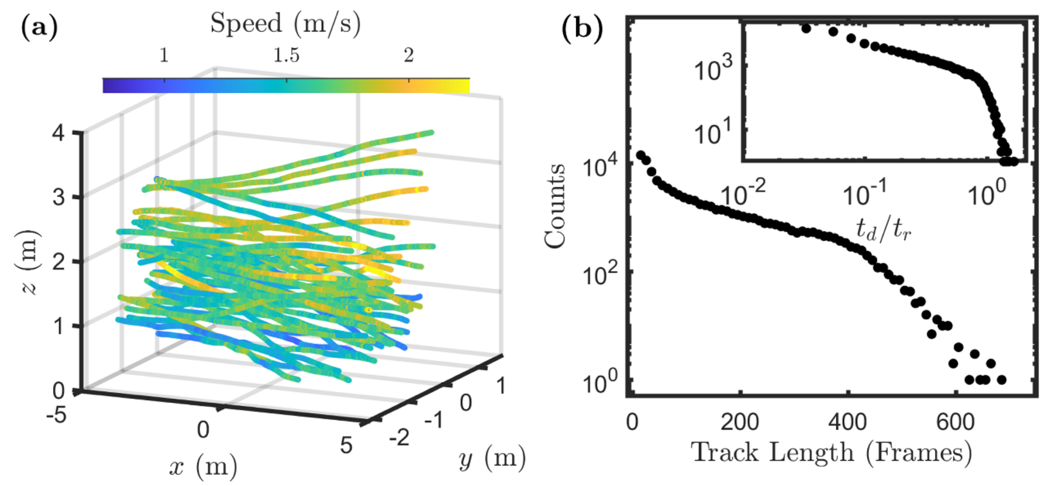

Figure 7. Example trajectories and track length distribution. (a) Fifty longest trajectories colored by speed. The x axis is aligned with the mean velocity and z with vertical. (b) Track length distribution in frames. Inset shows track length normalized by domain residence time, which limits the longest trajectories.

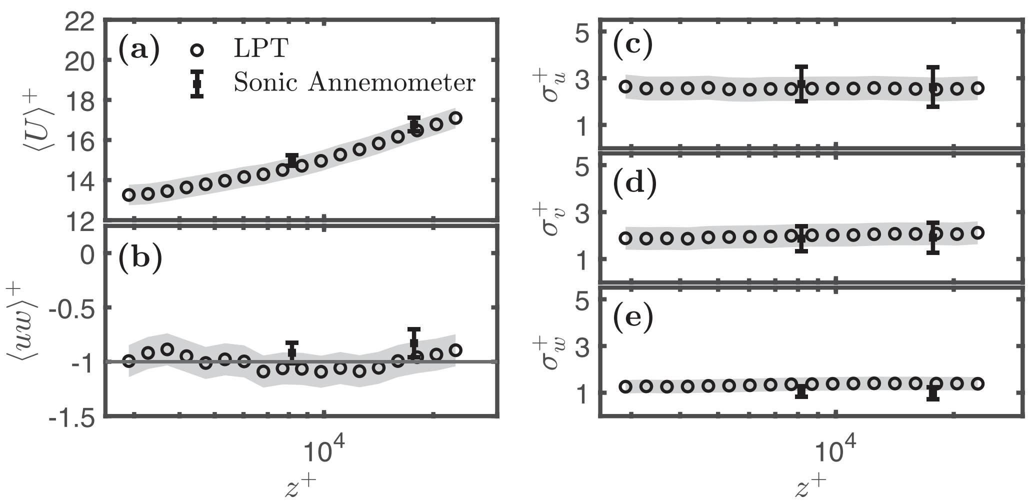

Figure 8. First and second order wall normal single point statistics. Shading indicates uncertainty for the LPT system.

indicates a constant failure rate. The tail of the distribution is limited by the particle residence time in the domain. An inset in figure 7(b) shows a log-log plot of the track length histogram. Track duration t_d is normalized by the domain residence time t_r. Residence time is estimated as the domain side length divided by the mean velocity. As the track length approaches the residence time, the histogram decays rapidly. Since long trajectories are crucial to Lagrangian statistics, this analysis shows how the domain can be sized for studying a desired range of Lagrangian time scales.

3.3. Wall-normal Eulerian statistics

Conventional ASL measurement techniques provide single-point Eulerian statistics. The LPT system provides a sparse snapshot of the flow field at every time instant, but the positions where the velocity is being measured are rarely sampled multiple times. By assuming the flow is statistically homogeneous and stationary, single-point statistics can be estimated, and compared to those derived from sonic anemometer measurements. Such a comparison is shown in figure 8. Wall-normal statistics are computed under the assumption that the flow is statistically homogeneous in the horizontal directions and stationary in time. A Gaussian weighted average is used to perform this conversion with points spaced logarithmically from the surface. Details on the conversion can be found in appendix C.

Wall-normal statistics in figure 8 are normalized by 'inner' scales. The friction velocity u_τ is estimated by assuming a constant stress layer. The friction velocity from LPT data is used to normalize both the sonic and LPT data. Shading indicates uncertainty based on the analysis in appendix B for the LPT system. Uncertainty in sonic anemometer statistics are estimated using the filtering method [47].

Measurements of the mean streamwise velocity in figure 8(a), streamwise standard deviation in figure 8(c), and spanwise standard deviation in figure 8(d) agree within the estimated uncertainty. Measurements of the

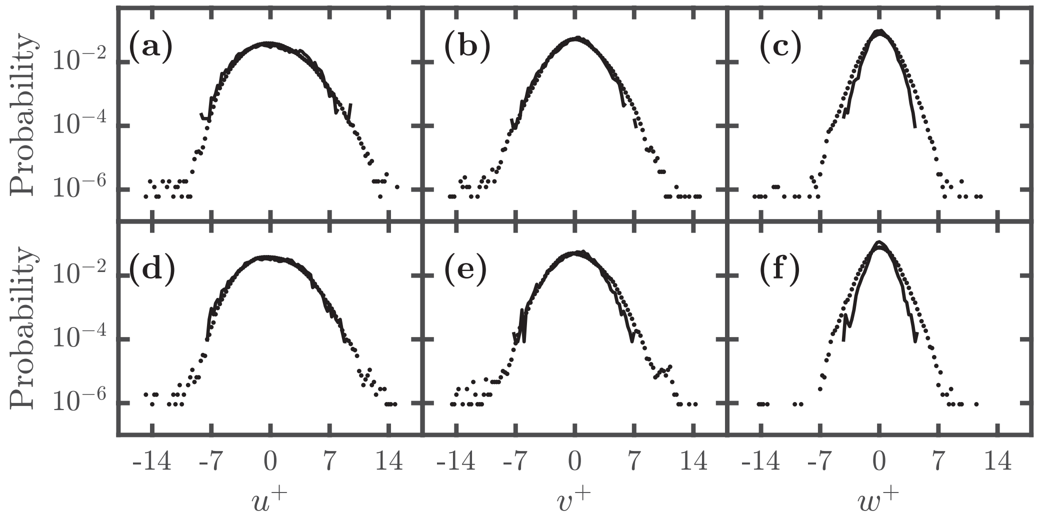

Figure 9. Probability distributions of velocity fluctuations from sonic (lines) and LPT system (markers) at two heights. (a)–(c) $z = 0.89$ (d)–(f) $z = 1.93$ m.

streamwise-vertical Reynolds stress in figure 8(b) and vertical velocity standard deviation in figure 8(e) are also consistent between the sonics and LPT system. However, there is a slight bias in the sonic measurements to lower magnitude values. This is plausibly attributed to path averaging, as the path length of the sonic anemometer is 10 cm, an order of magnitude larger than the bubble diameter. Energy-containing scales of vertical motions are expected to be smaller than the streamwise and spanwise directions because of the presence of the surface.

In figure 9, we show the probability distributions of velocity fluctuations measured by the sonic anemometers and the LPT system. All LPT velocity measurements within ± 0.2 m of the sonic heights are used to compute the distributions. For the streamwise (u) and spanwise (v) components excellent agreement is observed out to events with probability 10^{-4}. Measurements of low-probability events are limited by the number of observations. By averaging over horizontal planes the LPT system obtains approximately two orders of magnitude more observations than the sonic anemometers in the same time window, allowing estimation of events with very low probability. Even if low-probability events are not of interest, the statistical convergence is generally improved by more measurements. For example, the LPT-measured distributions vary smoothly up to probability 10^{-4} whereas the sonic distributions show clear signs of noise, e.g. in the right flank of figure 9(a). The LPT-measured vertical velocity (w) distribution is broader than the sonic-measured distribution, consistent with the difference in variance observed in figure 8(e). Thus the sonic and LPT comparisons generally validate the LPT system for Eulerian measurements, with small differences attributed to path averaging by the sonic anemometers.

3.4. Dispersion statistics

The Lagrangian view is natural for problems involving the spread of a passive tracer in the ASL [6]. Neglecting molecular diffusion, concentration is conserved along Lagrangian particle trajectories. To investigate this in the present data set displacement statistics from trajectories 1 ± 0.2 m above the ground are studied. The displacements mimic the spread of a passive scalar point source under the assumptions of stationary and homogeneity over the horizontal slice of the measurement domain. The assumption of homogeneity over heights of 1 ± 0.2 m is supported by the Eulerian statistics in the previous section. The mean velocity change over this vertical window is approximately 5.5% and changes in second-order statistics are less than 3%. Then, under the assumptions given, the probability distribution of displacements is proportional to the mean concentration distribution [48]. This is illustrated by the trajectories in figure 10(a).

Measurements of displacement statistics also highlight the range of scales resolved by the LPT system. Consider the displacement variances shown in figure 10(b). Measured displacement fluctuations are compared to Taylor's theory of dispersion for homogeneous stationary turbulence [49], with the early-time prediction shown in solid lines. At early times the displacement variances are predicted to grow ballistically, e.g. $\sigma_x^2 = \sigma_u^2 \Delta t^2$ for the streamwise direction. Displacement variances measured by the LPT system are larger than the prediction at short times because of positional noise, which has a non-negligible contribution to displacement fluctuations at very short times. As Δt increases the displacement fluctuations of fluid particles increase, thereby increasing the signal-to-noise ratio. The onset of measured ballistic scaling is consistent with the uncertainty analysis in appendix B. Positional uncertainties are approximately 3 mm and the approach to ballistic scaling occurs when displacement fluctuations exceed approximately 10 mm. Regardless of positional noise, scales smaller than the 8 mm particle diameter are not resolved due to finite-size effects. Nearly a decade of ballistic scaling is observed, emphasizing the ability of the LPT system to characterize small-scale statistics. As Δt further increases velocity fluctuations lose correlation and the displacement variance

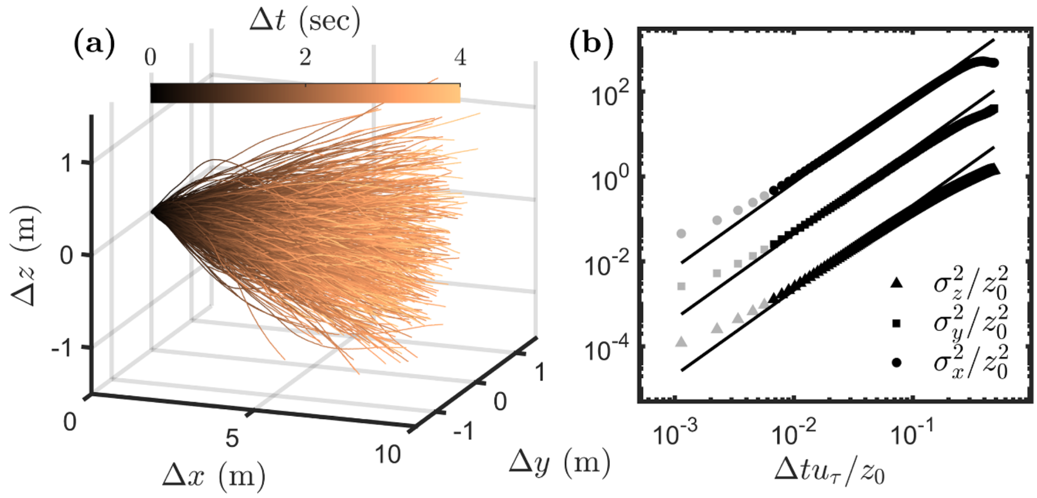

Figure 10. Dispersion results from field experiments for trajectories at $z_0 = 1$ m above the surface. (a) 1000 trajectories translated to a common origin and colored by time along the trajectory. (b) Measured mean squared displacements as a function of time difference (symbols). Solid lines are the short-time ballistic prediction. Curves for each component are shifted vertically for clarity. Gray points are contaminated by noise.

growth slows down. Measurements of this behavior are key to stochastic Lagrangian models, but current data are limited [6, 50]. The ability of the presented system to provide Lagrangian field measurements across a broad range of scales paramount to dispersion modeling is unprecedented.

4. Discussion and conclusion

We have presented a novel particle tracking system for measurements of Eulerian and Lagrangian statistics in the atmosphere. The system has been designed around the unique constraints of field experiments in the ASL. A balance is sought between flexibility, ease of use, and measurement accuracy. The system uses commercially available mirrorless cameras sampling at 4 K resolution and 120 Hz frame rate, 8 mm HFSBs and nine 500 W LEDs. Analysis relevant to the system design is presented, offering guidelines on image-based field measurements.

The system was evaluated in a field experiment where Eulerian and Lagrangian statistics were computed. Eulerian wall-normal statistics showed favorable comparisons to sonic anemometers in both mean velocities and fluctuations. Lagrangian dispersion statistics were assessed from particle tracks. Measured displacement fluctuations support Taylor's theory of dispersion [49] at early times. This early-time ballistic scaling is precisely the behavior that cannot be captured by eddy diffusivity closures [51], warranting further investigations of Lagrangian statistics in the ASL.

Data availability statement

The data that support the findings of this study are openly available at the following URL/DOI: https://doi.org/10.34770/rv5j-f229 [52].

Acknowledgments

The authors gratefully acknowledge Prof Elie Bou-Zeid for helpful discussions and providing the sonic anemometers. This work was partially funded by the National Science Foundation (NSF) under award number 2132727 as well as the Gordon and Betty Moore Foundation Under Grant number GBMF11572. N Conlin was partially supported by the New Jersey Economic Development Authority (NJEDA) Wind Institute Fellowship. NJ Wei was supported by the Andlinger Center for Energy and the Environment Distinguished Postdoctoral Fellowship.

Appendix A. Camera synchronization

This section describes the procedure to synchronize cameras using a multicolor light in the center of the measurement domain. The light color oscillates between blue, red, and green. Each color is held constant for approximately 0.17 s. The synchronizing light is visible to each camera, as shown in figure 6(a). Intensity time series of the synchronizing light are extracted from each camera by cropping the image around the light and summing the pixels. An example intensity time series is shown in figure A1(a). The light begins blue, switches to red, and then to green. A difference in the color switch timing between camera 1 and camera 2 can be seen. This difference implies a time offset between the two cameras. To quantify this offset the correlation coefficient between the intensity signal from each camera is computed at different time lags. The correlation coefficient computed by shifting the second camera's intensity signal is shown in figure A1(b). There is a clear peak at -4 frames in each color channel, indicating a 4 frame offset between the two cameras. An offset is computed this way for each camera and used to align the videos from different cameras. The offset calculation is done at the beginning and end of

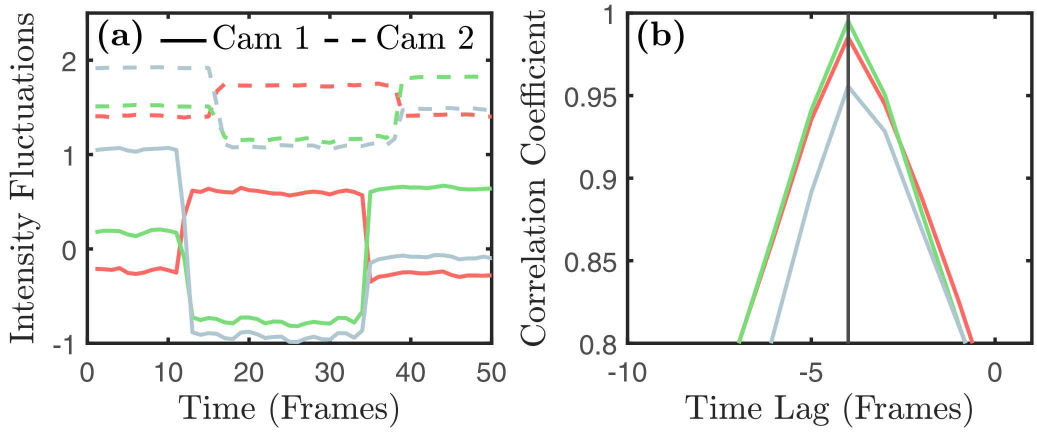

Figure A1. Illustration of synchronizing method. Colors correspond to the different color channels recorded by the camera (red, green, and blue). (a) Time series of intensity fluctuations in arbitrary units. The second camera time series (Cam 2) is shifted vertically for clarity. (b) Correlation coefficient between intensity from the first and second camera as a function of the second camera time shift. The vertical line is the estimated offset.

each video to test for any drift throughout the video. We find no drift.

The cross-correlation analysis described above can only synchronize the cameras within one frame. Smaller temporal misalignments cannot be detected. Residual lack of synchronization contributes to uncertainty in the triangulated particle positions. As discussed in section 2.6, particles are triangulated by matching the rays emanating from each camera. A lack of synchronization will increase the distance between rays that nominally intersect. The rays from one camera may be associated with the particle positions in the near past or future, relative to the other cameras. Since the triangulated particle positions are computed as the midpoint of nearly intersecting rays, the errors introduced by a lack of synchronization will manifest in reprojection errors, i.e. the rays from different cameras will not exactly intersect the particle position. Therefore the uncertainty introduced by any lack of synchronization is captured in the uncertainty analysis of appendix B.

Appendix B. Uncertainty analysis

This section describes the uncertainty analysis using variance propagation for the system based on a combination of calibration and particle reprojection errors introduced in [53]. These effects are combined to yield a 2D positional uncertainty in each camera. The 2D uncertainty is propagated to a 3D positional uncertainty by linearizing the camera calibration equations around 3D points, forming a matrix equation that couples the four camera calibrations [53].

The calibration for each camera provides a map from 3D position $\mathbf{x}$ to 2D camera coordinate $\mathbf{X}$ (in pixels) based on a set of calibration parameters $\mathbf{a}$, written as

$$\mathbf{X} = \mathbf{F}(\mathbf{x}, \mathbf{a}). \tag{B.1}$$

Uncertainties are assessed by linearizing the mapping function about the triangulated particle positions and fit calibration parameters. For small random perturbations to camera position $\delta\mathbf{X}$ and camera calibration parameters $\delta\mathbf{a}$ there is a resulting perturbation to the 3D position $\delta\mathbf{x}$ that we want to know. In Cartesian tensor notation, and using Einstein summation convention, equation (B.1) can be written as

$$\delta X_i = \frac{\partial F_i}{\partial x_j}\delta x_j + \frac{\partial F_i}{\partial a_j}\delta a_j. \tag{B.2}$$

Multiplying both sides of this equation by δX_k and averaging leads to an equation relating system co-variances

$$\langle \delta X_i \delta X_k \rangle + \frac{\partial F_i}{\partial a_j}\langle \delta a_j \delta a_l \rangle \frac{\partial F_k}{\partial a_l} = \frac{\partial F_i}{\partial x_j}\langle \delta x_j \delta x_l \rangle \frac{\partial F_k}{\partial x_l}. \tag{B.3}$$

Correlations between the calibration errors and 2D position errors have been neglected. In equation (B.3) the indices i and k each run from 1 to 2. The same equation can be written for all n_c cameras, leading to a matrix equation of size $2n_c \times 2n_c$ [53], that can be solved for 3D position covariances if the calibration uncertainty and 2D position uncertainty are known.

Calibration and 2D particle uncertainty are estimated using reprojection errors. 3D points are triangulated from 2D locations using the algorithm discussed in section 2.6. Identified 3D points are mapped back to the camera using B.1. The reprojection error, measured in pixels, is the difference between the mapped and the initially identified point. Using the identified wand endpoints from the calibration gives a typical calibration reprojection error for each camera that is approximately 0.5 pixels. Particle identification, residual lack of synchronization, and triangulation also introduce errors, quantified with reprojection errors. Histograms of particle reprojection errors are shown in figures B1(a)–(d). Particle reprojection errors generally make a larger contribution to the total 2D uncertainty than the calibration. Particle reprojection variances are summed with the calibration uncertainty for each camera and propagated via equation (B.3) to yield a 3D positional uncertainty at each triangulated point. The PDFs of 3D positional uncertainties in each direction are shown in figure B1. Here z is the vertical coordinate and x, y are the horizontal coordinates. Average uncertainties in each direction

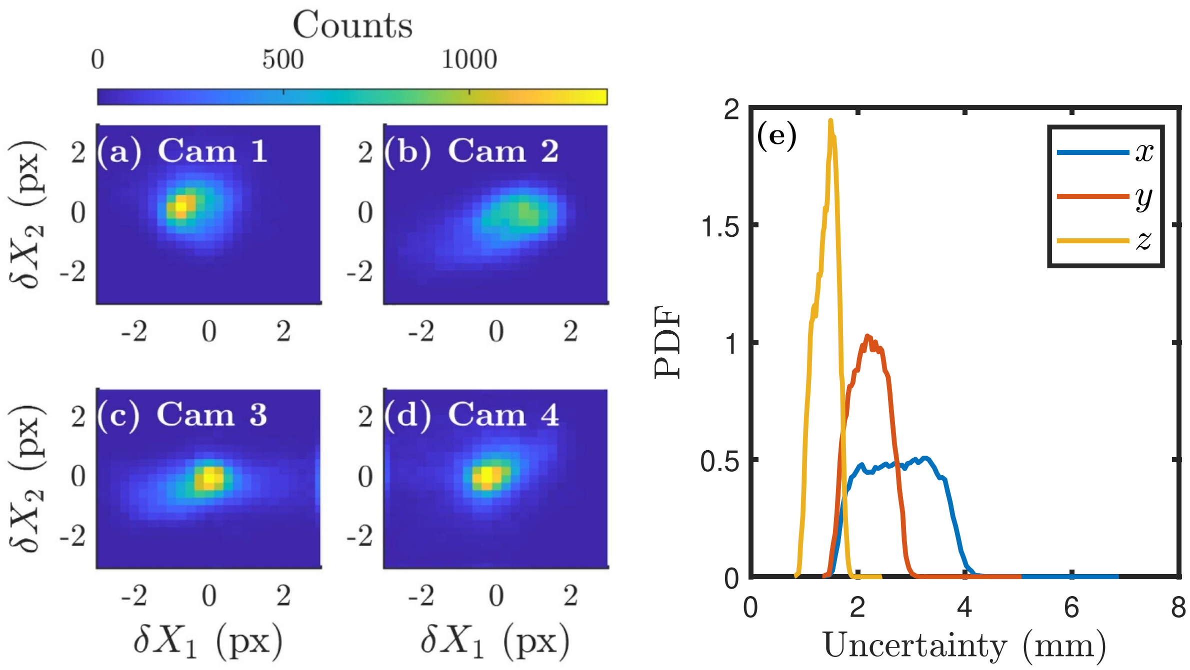

Figure B1. Uncertainty analysis. 2D reprojection errors in (a)–(d) are combined with the calibration reprojection uncertainty and propagated to 3D position uncertainties (e) by linearizing the calibration equations.

are $e_x = 2.8\,\text{mm}$, $e_y = 2.2\,\text{mm}$, and $e_z = 1.4\,\text{mm}$. Uncertainties have not been reported in most previous field LPT experiments, but [16] reports a 10 mm uncertainty from the calibration alone. Velocity uncertainty is determined by creating artificial trajectories with a known velocity, introducing Gaussian 3D positional errors according to the previous analysis, and comparing the noisy estimated velocity to the known velocity. The results are velocity uncertainties of $e_u = 7.5\,\text{cm}\,\text{s}^{-1}$, $e_v = 6.0\,\text{cm}\,\text{s}^{-1}$, and $e_w = 3.9\,\text{cm}\,\text{s}^{-1}$.

Appendix C. Lagrangian to Eulerian conversion: single-point statistics

Differentiation of the particle tracks produces an unstructured grid of velocity measurements at each time step. To make comparisons to conventional Eulerian measurements, which are taken at a fixed location, the velocity measurements from particle tracks are binned and averaged using a Gaussian weight function [36, 54]. This approach has the added benefit of improving statistical convergence [54]. For each point, $\mathbf{p}$ where Eulerian statistics are desired a bin is drawn. The bin $\mathcal{B}_p$ is a rectangular prism centered on $\mathbf{p}$ with half-widths δ_x, δ_y, and δ_z in the three coordinate directions. The desired statistics are computed as a weighted average for all measurements within $\mathcal{B}_p$. Each $\mathbf{p}$ has an associated Gaussian weight function $w_p(\mathbf{x}) : \mathbb{R}^3 \to [0,1]$ defined by

$$w_p(\mathbf{x}) = \begin{cases} \exp\left(-(\mathbf{x}-\mathbf{p})^T \mathbf{C}^{-1}(\mathbf{x}-\mathbf{p})\right) & \mathbf{x} \in \mathcal{B}_p \\ 0 & \mathbf{x} \notin \mathcal{B}_p \end{cases} \tag{C.1}$$

where $\mathbf{C} \in \mathbb{R}^{3\times 3}$ is a diagonal matrix. The values of $\mathbf{C}$ are set by forcing the weight function to achieve a particular value on the bin boundary. For example, the first element of $\mathbf{C}$ on the main diagonal is set by requiring $w_p(\mathbf{p} + \delta_x \hat{\mathbf{i}}) = c_x$. Here $\hat{\mathbf{i}}$ is the unit vector aligned with the x axis and c_x is a constant between 0 and 1 that specifies how quickly the weight function decays away from the bin center in the $\hat{\mathbf{i}}$ direction. The lower the value of c_x the faster the decay. The same procedure is used to set the weight function decay in other coordinate system directions using the widths δ_y and δ_z and the constants c_y and c_z.

Average quantities at the desired points can be computed for a set of particle trajectories and specified weight functions. This involves averaging measurements of the instantaneous velocity $\mathbf{U}(\mathbf{x},t)$ from particle tracks. The two primary quantities of interest are the mean velocity $\langle \mathbf{U} \rangle(\mathbf{x})$ and the Reynolds stress tensor $\langle \mathbf{uu} \rangle(\mathbf{x})$. The Reynolds stress tensor is composed of the variances and covariances of the velocity fluctuations $\mathbf{u} = \mathbf{U} - \langle \mathbf{U} \rangle$. Formally, the average velocity at the point $\mathbf{p}$ from all n_m measurements of the instantaneous velocity at points $\mathbf{m}_i$ is computed as

$$\langle \mathbf{U} \rangle (\mathbf{p}) = \frac{\sum_{i=1}^{n_m} w_p(\mathbf{m}_i)\, \mathbf{U}(\mathbf{m}_i, t)}{\sum_{i=1}^{n_m} w_p(\mathbf{m}_i)}. \tag{C.2}$$

In practice measurements outside of the bin are discarded and the average is computed over the remaining samples. The weighting only depends on the distance from the measurement point and all times are treated equally. Once the mean velocity is determined then the Reynolds stress tensor can be calculated by subtracting the mean velocity from all measurements in the bin and averaging according to equation (C.2).

The statistics presented in figure 8 are computed for 18 logarithmically spaced from $10^{-0.5}$ m to $10^{0.4}$ m. Decay constants are the same at all points with $c_x = c_y = 0.9$ and $c_z = 0.1$. The horizontal bin widths are $\delta_x = \delta_y = 8\,\text{m}$. Vertical bin widths are set so that the bottom bin surface is at the same height as the point below. That is, labeling the measurement points by increasing height above the surface, $\delta_z^i = z_i - z_{i-1}$. The first point has $\delta_z^1 = z_1$. The bin spacing and size were set so that the minimum number of samples contributing to each bin is approximately 10^5. The actual minimum number of samples is 0.93×10^5 and the average is 7.4×10^5.

ORCID iDs

Nicholas Conlin https://orcid.org/0009-0003-4717-4593
Nathaniel J Wei https://orcid.org/0000-0001-5846-6485
N Agastya Balantrapu https://orcid.org/0000-0002-5641-4566
Marcus Hultmark https://orcid.org/0000-0002-5070-3711

References

[1] Calaf M, Vercauteren N, Katul G, Giometto M G, Morrison T J, Margairaz F, Boyko V and Pardyjak E R 2023 Boundary-layer processes hindering contemporary numerical weather prediction models *Boundary-Layer Meteorol.* **186** 43–68
[2] Stevens R J A M and Meneveau C 2017 Flow structure and turbulence in wind farms *Annu. Rev. Fluid Mech.* **49** 311–39
[3] Porté-Agel F, Bastankhah M and Shamsoddin S 2020 Wind-turbine and wind-farm flows: a review *Boundary-Layer Meteorol.* **174** 1–59
[4] Reddy G, Murthy V N and Vergassola M 2022 Olfactory sensing and navigation in turbulent environments *Annu. Rev. Condens. Matter Phys.* **13** 191–213
[5] Stull R B 1988 *An Introduction to Boundary Layer Meteorology* (Springer)
[6] Rodean H C 1996 *Stochastic Lagrangian Models of Turbulent Diffusion* (American Meteorological Society)
[7] Pope S B 1994 On the relationship between stochastic Lagrangian models of turbulence and second-moment closures *Phys. Fluids* **6** 973–85
[8] Shnapp R, Liberzon A, Bohbot-Raviv Y and Fattal E 2024 On local isotropy and scale dependence of pair dispersion in turbulent canopy flows *J. Fluid Mech.* **978** A3
[9] Schröder A and Schanz D 2023 3D Lagrangian particle tracking in fluid mechanics *Annu. Rev. Fluid Mech.* **55** 511–40
[10] Discetti S and Coletti F 2018 Volumetric velocimetry for fluid flows *Meas. Sci. Technol.* **29** 042001
[11] Theriault D H, Fuller N W, Jackson B E, Bluhm E, Evangelista D, Wu Z, Betke M and Hedrick T L 2014 A protocol and calibration method for accurate multi-camera field videography *J. Exp. Biol.* **217** 1843–8
[12] Hong J, Toloui M, Chamorro L P, Guala M, Howard K, Riley S, Tucker J and Sotiropoulos F 2014 Natural snowfall reveals large-scale flow structures in the wake of a 2.5–MW wind turbine *Nat. Commun.* **5** 4216
[13] Heisel M, Dasari T, Liu Y, Hong J, Coletti F and Guala M 2018 The spatial structure of the logarithmic region in very-high-Reynolds-number rough wall turbulent boundary layers *J. Fluid Mech.* **857** 704–47
[14] Bristow N, Li J, Hartford P, Guala M and Hong J 2023 Imaging-based 3D particle tracking system for field characterization of particle dynamics in atmospheric flows *Exp. Fluids* **64** 1–14
[15] Wei N J, Brownstein I D, Cardona J L, Howland M F and Dabiri J O 2021 Near-wake structure of full-scale vertical-axis wind turbines *J. Fluid Mech.* **914** A17
[16] Rosi G A, Sherry M, Kinzel M and Rival D E 2014 Characterizing the lower log region of the atmospheric surface layer via large-scale particle tracking velocimetry *Exp. Fluids* **55** 1736
[17] Voth G A, La Porta A, Crawford A M, Alexander J and Bodenschatz E 2002 Measurement of particle accelerations in fully developed turbulence *J. Fluid Mech.* **469** 121–60
[18] Adrian R J and Westerweel J 2011 *Particle Image Velocimetry* (Cambridge University Press)
[19] Mei R 1996 Velocity fidelity of flow tracer particles *Exp. Fluids* **22** 1–13
[20] Faleiros D E, Tuinstra M, Sciacchitano A and Scarano F 2021 The slip velocity of nearly neutrally buoyant tracers for large-scale PIV *Exp. Fluids* **62** 186
[21] Maxey M R and Riley J J 1983 equation of motion for a small rigid sphere in a nonuniform flow *Phys. Fluids* **26** 883–9
[22] Auton T R, Hunt J C R and Prud'Homme M 1988 The force exerted on a body in inviscid unsteady non-uniform rotational flow *J. Fluid Mech.* **197** 241–57
[23] Melling A 1997 Tracer particles and seeding for particle image velocimetry *Meas. Sci. Technol.* **8** 1406–16
[24] Hjelmfelt A T and Mockros L F 1966 Motion of discrete particles in a turbulent fluid *Appl. Sci. Res.* **16** 149–61
[25] Qureshi N M, Bourgoin M, Baudet C, Cartellier A and Gagne Y 2007 Turbulent transport of material particles: an experimental study of finite size effects *Phys. Rev. Lett.* **99** 184502
[26] Calzavarini E, Volk R, Bourgoin M, Lévêque E, Pinton J F and Toschi F 2009 Acceleration statistics of finite-sized particles in turbulent flow: the role of Faxén forces *J. Fluid Mech.* **630** 179–89
[27] Brown R D, Warhaft Z and Voth G A 2009 Acceleration statistics of neutrally buoyant spherical particles in intense turbulence *Phys. Rev. Lett.* **103** 194501
[28] Volk R, Calzavarini E, Lévêque E and Pinton J F 2011 Dynamics of inertial particles in a turbulent von Kármán flow *J. Fluid Mech.* **668** 223–35
[29] Pope S B 2000 *Turbulent Flows* (Cambridge University Press)
[30] Freire L S, Dias N L and Chamecki M 2019 Effects of path averaging in a sonic anemometer on the estimation of turbulence-kinetic-energy dissipation rates *Boundary-Layer Meteorol.* **173** 99–113
[31] Scarano F, Ghaemi S, Caridi G C A, Bosbach J, Dierksheide U and Sciacchitano A 2015 On the use of helium-filled soap bubbles for large-scale tomographic PIV in wind tunnel experiments *Exp. Fluids* **56** 42
[32] Faleiros D E, Tuinstra M, Sciacchitano A and Scarano F 2018 Helium-filled soap bubbles tracing fidelity in wall-bounded turbulence *Exp. Fluids* **59** 56
[33] Gibeau B and Ghaemi S 2018 A modular 3D-printed helium-filled soap bubble generator for large-scale volumetric flow measurements *Exp. Fluids* **59** 1–11
[34] Gibeau B, Gingras D and Ghaemi S 2020 Evaluation of a full-scale helium-filled soap bubble generator *Exp. Fluids* **61** 1–18
[35] Grille Guerra A, Scarano F and Sciacchitano A 2024 On the scalability of helium-filled soap bubbles for volumetric PIV *Exp. Fluids* **65** 1–17
[36] Faleiros D E, Tuinstra M, Sciacchitano A and Scarano F 2019 Generation and control of helium-filled soap bubbles for PIV *Exp. Fluids* **60** 40
[37] Ni R 2024 Deformation and breakup of bubbles and drops in turbulence *Annu. Rev. Fluid Mech.* **56** 319–47
[38] Sane A, Mandre S and Kim I 2018 Surface tension of flowing soap films *J. Fluid Mech.* **841** R2
[39] Adrian R J 1991 Particle-imaging techniques for experimental fluid mechanics *Annu. Rev. Fluid Mech.* **23** 261–304
[40] Hou J, Kaiser F, Sciacchitano A and Rival D E 2021 A novel single-camera approach to large-scale, three-dimensional

particle tracking based on glare-point spacing *Exp. Fluids* **62** 100

[41] Ouellette N T, Xu H and Bodenschatz E 2006 A quantitative study of three-dimensional Lagrangian particle tracking algorithms *Exp. Fluids* **40** 301–13

[42] Muller K, Hemelrijk C K, Westerweel J and Tam D S W 2020 Calibration of multiple cameras for large-scale experiments using a freely moving calibration target *Exp. Fluids* **61** 1–12

[43] Bourgoin M and Huisman S G 2020 Using ray-traversal for 3D particle matching in the context of particle tracking velocimetry in fluid mechanics *Rev. Sci. Instrum.* **91** 085105

[44] Schanz D, Schröder A, Gesemann S, Michaelis D and Wieneke B 2013 Shake The Box ‘: a highly efficient and accurate tomographic particle tracking velocimetry (TOMO-PTV) method using prediction of particle positions *10th Int. Symp. on Particle Image Velocimetry - PIV13* (*Delft, The Netherlands*) pp 1–13

[45] Mordant N, Crawford A M and Bodenschatz E 2004 Experimental Lagrangian acceleration probability density function measurement *Physica* D **193** 245–51

[46] Biferale L, Bodenschatz E, Cencini M, Lanotte A S, Ouellette N T, Toschi F and Xu H 2008 Lagrangian structure functions in turbulence: a quantitative comparison between experiment and direct numerical simulation *Phys. Fluids* **20** 065103

[47] Salesky S T, Chamecki M and Dias N L 2012 Estimating the random error in eddy-covariance based fluxes and Other turbulence statistics: the filtering method *Boundary-Layer Meteorol.* **144** 113–35

[48] Monin A S and Yaglom A M 1971 *Statistical Fluid Mechanics: Mechanics of Turbulence vol 1* (MIT Press) english ed. updated, augmented and rev edn

[49] Taylor G I 1922 Diffusion by Continuous Movements *Proc. Math. Soc.* **s2–20** 196–212

[50] Cassiani M, Bertagni M B, Marro M and Salizzoni P 2020 Concentration Fluctuations from Localized Atmospheric Releases *Boundary-Layer Meteorol.* **177** 461–510

[51] Thomson D J and Wilson J D 2012 History of Lagrangian stochastic models for turbulent dispersion *Lagrangian Modeling of the Atmosphere* (American Geophysical Union (AGU)) pp 19–36

[52] Conlin N *et al* 2024 Data for ‘Lagrangian Particle Tracking in the Atmospheric Surface Layer’ (https://doi.org/10.34770/rv5j-f229)

[53] Bhattacharya S and Vlachos P 2020 Volumetric particle tracking velocimetry (PTV) uncertainty quantification *Exp. Fluids* **61** 197

[54] Godbersen P and Schröder A 2020 Functional binning: improving convergence of Eulerian statistics from Lagrangian particle tracking *Meas. Sci. Technol.* **31** 095304